



HAL
open science

Stratospheric balloon observations of infrasound waves from the January 15 2022 Hunga eruption, Tonga

Aurélien Podglajen, Alexis Le Pichon, Raphaël Garcia, Solène Gérier,
Christophe Millet, Kristopher Bedka, Konstantin Khlopenkov, Sergey
Khaykin, Albert Hertzog

► To cite this version:

Aurélien Podglajen, Alexis Le Pichon, Raphaël Garcia, Solène Gérier, Christophe Millet, et al.. Stratospheric balloon observations of infrasound waves from the January 15 2022 Hunga eruption, Tonga. *Geophysical Research Letters*, 2022, 49 (19), pp.e2022GL100833. 10.1029/2022GL100833. insu-03790705

HAL Id: insu-03790705

<https://insu.hal.science/insu-03790705>

Submitted on 26 Oct 2022

HAL is a multi-disciplinary open access archive for the deposit and dissemination of scientific research documents, whether they are published or not. The documents may come from teaching and research institutions in France or abroad, or from public or private research centers.

L'archive ouverte pluridisciplinaire **HAL**, est destinée au dépôt et à la diffusion de documents scientifiques de niveau recherche, publiés ou non, émanant des établissements d'enseignement et de recherche français ou étrangers, des laboratoires publics ou privés.



Distributed under a Creative Commons Attribution - NonCommercial 4.0 International License

Geophysical Research Letters[®]

RESEARCH LETTER

10.1029/2022GL100833

Key Points:

- Comparison between balloon-borne and ground-based observations of infrasound waves triggered by the January 2022 Hunga eruption
- Eruption sequence from infrasound in broad agreement with plume top height evolution
- Benchmark for long-range monitoring of infrasound from large explosive sources using stratospheric balloon observations

Supporting Information:

Supporting Information may be found in the online version of this article.

Correspondence to:

A. Podglajen,
aurelien.podglajen@lmd.ipsl.fr

Citation:

Podglajen, A., Le Pichon, A., Garcia, R. F., G erier, S., Millet, C., Bedka, K., et al. (2022). Stratospheric balloon observations of infrasound waves from the 15 January 2022 Hunga eruption, Tonga. *Geophysical Research Letters*, 49, e2022GL100833. <https://doi.org/10.1029/2022GL100833>

Received 15 AUG 2022
Accepted 22 SEP 2022

  2022 The Authors.
This is an open access article under the terms of the [Creative Commons Attribution-NonCommercial License](https://creativecommons.org/licenses/by-nc/4.0/), which permits use, distribution and reproduction in any medium, provided the original work is properly cited and is not used for commercial purposes.

Stratospheric Balloon Observations of Infrasound Waves From the 15 January 2022 Hunga Eruption, Tonga

Aur lien Podglajen¹ , Alexis Le Pichon² , Rapha l F. Garcia³ , Sol ne G erier³,
Christophe Millet², Kristopher Bedka⁴ , Konstantin Khlopenkov⁵ , Sergey Khaykin⁶ , and
Albert Hertzog⁷

¹Laboratoire de M t eorologie Dynamique (LMD/IPSL),  cole Polytechnique, Institut Polytechnique de Paris, Sorbonne Universit ,  cole Normale Sup rieure, PSL Research University, CNRS, Paris, France, ²CEA, DAM, DIF, Arpajon, France, ³Institut Sup rieur de l'A ronautique et de l'Espace (ISAE-SUPAERO), Universit  de Toulouse, Toulouse, France, ⁴NASA Langley Research Center, Hampton, VA, USA, ⁵Science Systems and Applications, Inc, Hampton, VA, USA, ⁶Laboratoire Atmosph res, Observations Spatiales (LATMOS), UVSQ, Sorbonne Universit , CNRS, IPSL, Guyancourt, France, ⁷Laboratoire de M t eorologie Dynamique (LMD/IPSL), Sorbonne Universit ,  cole polytechnique, Institut polytechnique de Paris,  cole normale sup rieure, PSL Research University, CNRS, Paris, France

Abstract The 15 January 2022 eruption of the Hunga volcano (Tonga) generated a rich spectrum of waves, some of which achieved global propagation. Among numerous platforms monitoring the event, two stratospheric balloons flying over the tropical Pacific provided unique observations of infrasonic wave arrivals, detecting five complete revolutions. Combined with ground measurements from the infrasound network of the International Monitoring System, balloon-borne observations may provide additional constraint on the scenario of the eruption, as suggested by the correlation between bursts of acoustic wave emission and peaks of maximum volcanic plume top height. Balloon records also highlight previously unobserved long-range propagation of infrasound modes and their dispersion patterns. A comparison between ground- and balloon-based measurements emphasizes superior signal-to-noise ratios onboard the balloons and further demonstrates their potential for infrasound studies.

Plain Language Summary The eruption of the Hunga volcano on 15 January 2022 was one of the most powerful blasts of the last century. This fast and strong perturbation of the atmosphere triggered atmospheric waves which were followed around the world multiple times. Here, we use records of sound waves emitted by the eruption from two balloons flying at about 20 km altitude over the Pacific combined with ground stations around the volcano to help characterize the event and its scenario. Due to weak relative wind and turbulence, the sounds on the balloon are generally clearer than on the ground, demonstrating the potential of high-altitude measurements for extreme events.

1. Introduction

Started in mid-December 2021, the 2021–2022 eruption of Hunga volcano (Tonga) culminated on 15 January 2022 with an intense explosion around 04:16 UTC (Poli & Shapiro, 2022). Over the next hour, the volcanic plume penetrated deep into the atmosphere, reaching the stratopause and beyond (up to 58 km), whereas the umbrella cloud spread at approximately 35 km to form a 600 km diameter disk (Carr et al., 2022; Proud et al., 2022). The altitude of volcanic overshoots, the height and extent of the umbrella cloud set a new record for volcanic eruptions over the satellite era, overtaking Mount Pinatubo and its maximum reported plume height of 40 km (Holasek et al., 1996). The plume generated a large perturbation of the stratospheric aerosol layer and stratospheric composition (Mill n et al., 2022), with likely substantial radiative impacts (Sellitto et al., 2022).

Besides triggering globally detected surface seismic waves (Poli & Shapiro, 2022) and tsunamis in several oceanic basins (Matoza et al., 2022; Yuen et al., 2022), the Hunga eruption also excited a wide spectrum of atmospheric waves, which were observed radiating away from the volcano (Matoza et al., 2022). These include the edge Lamb wave (Matoza et al., 2022; Wright et al., 2022), internal gravity waves (Ern et al., 2022; Wright et al., 2022) and infrasound (Matoza et al., 2022; Vergoz et al., 2022). The Lamb wave amplitude (>11 hPa peak-to-peak near Hunga) and propagation pattern are in particular reminiscent of the wave trains observed following the historical 1883 Krakatoa eruption (Matoza et al., 2022).

Table 1
Receiver Coordinates and Infrasound Properties in Ground-Based and Balloon-Based Records

Receiver	Distance (km)	Latitude °N	Longitude °E	Altitude (km)	c_g (m/s)	Observed T_L (30–40 mHz) with respect to IS22 (dB)		
						WP1	WP2	WP3
IS07	5,227	−19.93	134.33	Ground	297.00	−15.66	−14.04	−37.19
IS22	1,849	−22.18	166.85	Ground	297.00	0.00	0.00	0.00
IS24	2,755	−17.75	−149.30	Ground	261.00	−28.27	ND	ND
IS36	2,699	−43.92	176.48	Ground	300.00	−15.82	−16.02	−28.11
IS40	3,957	−4.10	152.10	Ground	301.00	−22.72	−15.89	−28.67
ISS7	8,645	33.61	−116.45	Ground	292.00	−35.72	−23.67	−33.18
STR1	2,238	−0.80	−171.64	20.5	279.00	−14.89	−12.68	−24.75
TTL4	7,640	15.70	−116.02	18.5	276.00	−26.41	−22.75	−36.62

Note. ND: Wavepacket not discernible at receiver.

Most observations of Hunga waves were obtained by remote-sensing instruments or surface (micro)barometers, whereas the plume extended above stratospheric altitudes. In this paper, we present unique measurements of infrasound wave trains recorded in the stratosphere onboard two long-duration balloons flying over the Pacific. While balloon-borne instruments also detected acoustic signals corresponding to the early eruptive sequence of Hunga, including the January 13 explosion, the present study focuses on analyzing the waves triggered by the main eruption on January 15. We describe the first and multiple-revolution wave arrivals in balloon records and compare them with ground-based observations. Then, we discuss how infrasound may provide additional information on the eruption chronology and the value of balloon-borne measurements for this and similar events.

2. Data and Methods

2.1. Strateole-2 Balloon Data

In the frame of the Strateole-2 project (Haase et al., 2018), 17 superpressure balloons (SPBs) were launched from Seychelles by the French space agency (CNES) in October–December 2021. Strateole-2 SPBs are constant-volume balloons designed to fly several months at a chosen density level in the tropical upper troposphere-lower stratosphere (UTLS) (between 18.5 and 21 km altitude). On 15 January 2022, two SPBs (STR1 and TTL4) remained over the tropical Pacific at about 19 km above sea level (a.s.l). Their altitudes and approximate locations are given in Table 1 and displayed in Figure 1a). Both balloons drifted horizontally following the wind, which for infrasound waves implies negligible Doppler shift but changes the distance to source with time.

Among various instruments, all Strateole-2 payloads notably include the TSEN temperature and pressure sensors (Hertzog et al., 2007) and a GPS. Position is measured every 30 s with 1 m altitude resolution. The pressure sensor (Paroscientific-6000-15A) samples at 1 Hz with 100 μ Pa resolution. It has a flat frequency response over the range of interest (up to 0.25 Hz).

SPBs undergo vertical oscillations forced by atmospheric motions and modulated by the balloon's response (Massman, 1978; Vincent & Hertzog, 2014). Due to the background vertical pressure gradient, such vertical motions induce additional apparent pressure fluctuations compared to measurements obtained at constant altitude. To correct for this effect, we remove the component of pressure fluctuations due to the hydrostatic pressure gradient in order to derive the Eulerian (constant-altitude) pressure perturbation p :

$$p = p_l \exp\left(\frac{g}{R_d T} \zeta'\right) - \bar{p}_l \quad (1)$$

where p_l and T are the raw (balloon-following) pressure and temperature, \bar{p}_l the time-averaged pressure, ζ' geopotential height anomalies, $g = 9.81 \text{ m s}^{-2}$ and $R_d = 287 \text{ J/K/kg}$. GPS altitude is interpolated at 1 s to compute ζ' and p . The effect of correction 1, described in Supporting Information S1, is significant at frequencies around that of

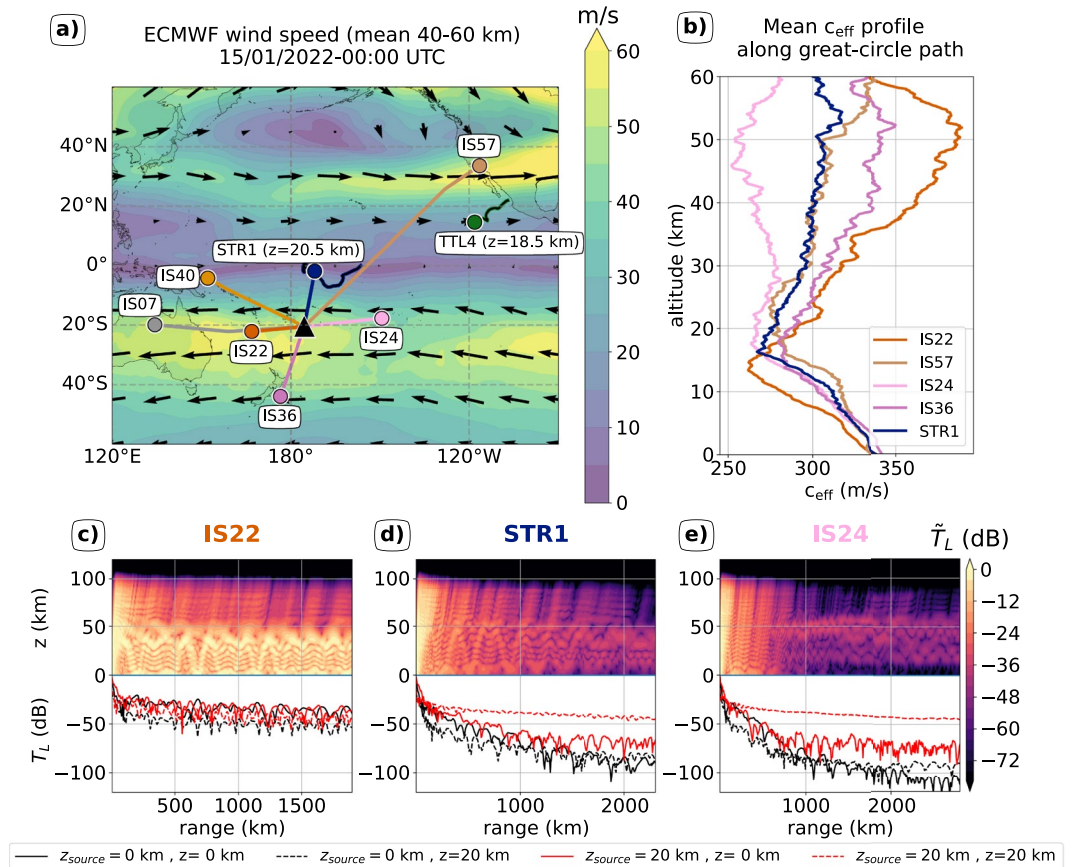


Figure 1. (a) Upper-stratospheric (40–60 km average) horizontal wind direction (vectors) and speed (contours) on 15 January 2022 from European Center for Medium-range Weather Forecast (ECMWF). Colored dots represent the location of the ground stations and balloons at the time of the main blast, with (colored lines) Hunga-to-receiver orthodromes. Balloon trajectories starting from the 15 January eruption until the termination of the flights are shown in black. (b) Average effective sound speed profile along selected orthodromes in (a). Panels (c–e) (top) Along-path sections of scaled transmission loss \tilde{T}_L with respect to $d_r = 17.5$ km, $z_r = z_{source}$ in the directions of IS22, STR1, and IS21 computed for a source of frequency 0.05 Hz located at the ground. (Bottom) Transmission loss profiles T_L at the ground (solid lines) and 20 km a.s.l. (dashed lines) for a point source at the ground (black) and 20 km a.s.l. (red).

the balloon oscillations (~ 4.5 mHz) or lower, but for infrasound frequencies above ~ 0.02 Hz, p closely follows p_t . The precision of the pressure data is sufficient to detect the energy peak of the oceanic microbarom around 0.2 Hz (Bowman & Lees, 2018).

2.2. IMS Microbarometer Data

Infrasound stations from the International Monitoring System (IMS) of the Comprehensive Nuclear-Test-Ban Treaty Organization are arrays of microbarometers sensitive to acoustic pressure variations between 0.02 and 4 Hz with a flat frequency response (e.g., Hupe et al., 2022). We use data from 6 stations listed in Table 1 and located either in the vicinity of the balloons or at distances of 1,800–4,000 km from Hunga (Figure 1a). A thorough investigation of Hunga infrasound waves in IMS data is presented in Vergoz et al. (2022).

2.3. Ancillary Data Set: Geostationary Satellite Data

We also employ 10-min-resolution stereoscopic cloud top height (CTH) retrievals to infer the chronology of the eruption. These data are derived at NASA Langley using the parallax between almost-synchronized 10.3 μm -band brightness temperature images obtained from different viewing angles by the geostationary satellites GOES-17 (Eastern Pacific sector) and Himawari-8 (Western Pacific sector). For the Hunga plume, the spatial

resolution of the product is about 6 km and its vertical accuracy typically lies between 0.2 and 0.4 km. Further description of the retrieval method is provided in Text S2 of Supporting Information S1.

2.4. Numerical Simulations of Infrasound Attenuation

In a horizontally isotropic medium, the modulus $|P|$ of (ducted) wave pressure amplitude varies along propagation path due to geometric spreading, following (e.g., Pierce & Posey, 1971):

$$|P|(d, z) = \sqrt{\frac{\rho(z) \sin(d_r/a)}{\rho_r \sin(d/a)}} |\tilde{P}|(z) \quad (2)$$

where a is the Earth radius, d the horizontal distance (range) from Hunga (d_r , an arbitrary reference distance), ρ the density, ρ_r a reference density ($\rho_r = 1.2 \text{ kg/m}^3$ except if stated otherwise) and the density- and range-scaled pressure amplitude $|\tilde{P}|$ a priori depends only on altitude z . Note that the vertical scaling in Equation 2 only retains the density factor in sonic impedance $I = \rho c$, since variations of the sound speed factor c are overshadowed by the vertical structure of the mode for long-range horizontal propagation. Equation 2 also neglects leakage and absorption. Most importantly, the assumed isotropic propagation breaks for infrasound waves which are particularly sensitive to the stratospheric wind field (Matoza et al., 2022; Vergoz et al., 2022).

To gain insight into the expected evolution of infrasound amplitude with range for different azimuths, we compute (linear) attenuation at a frequency of $f = 0.05 \text{ Hz}$ using the range-dependent parabolic equation (PE) solver NCPA-ePape (Waxler et al., 2021). The model assumes planar propagation along the orthodromes and the influence of wind is encapsulated into an effective sound celerity c_{eff} . c_{eff} sections along each great-circle path are defined by:

$$c_{\text{eff}}(d, z) = \sqrt{\gamma R_d T(d, z) + \mathbf{u}_h(d, z) \cdot \mathbf{e}_x(d, z)}, \quad (3)$$

with $\gamma = 7/5$ the heat capacity ratio, T the temperature, \mathbf{u}_h the horizontal wind vector and \mathbf{e}_x the range-dependent unit vector pointing from the source toward the receiver. c_{eff} profiles, calculated from the European Center for Medium-range Weather Forecast (ECMWF) ERA5 reanalysis (Hersbach et al., 2020), are shown in Figure 1b. Above 60 km and up to 140 km, ECMWF profiles are merged with temperature and wind climatologies (MSISE00 and HWM14, Picone et al., 2002; Drob et al., 2015) perturbed by a range-dependent realization of a gravity-wave field prescribed following Gardner et al. (1993). For the lower boundary condition, we assume a rigid ground (infinite impedance). Transmission losses (T_L) between Hunga and the sensors are quantified in dB, that is:

$$T_L(d, z) = 20 \log_{10} \left(\frac{|P|(d, z)}{|P|(d = d_r, z = z_r)} \right) \quad (4)$$

where z and z_r are the receiver and reference altitude. Figures 1c–1e presents sections of scaled transmission loss \tilde{T}_L (calculated using scaled pressure $|\tilde{P}|$ in place of $|P|$ in Equation 4) and curves of regular T_L (using $|P|$) from NCPA-ePape. Results highlight expected anisotropic propagation. In the spirit of comparing signal-to-noise ratios (SNR) onboard balloons and on the ground, keeping the $\rho^{-1/2}$ factor has its merits, since possible sources of dynamical noise at high altitude (i.e., balloon or gondola wake encounters) scale with density and dominate over altitude-independent electronic noise (Krishnamoorthy et al., 2020).

Note that, as stressed by Matoza et al. (2022), directly interpreting Hunga infrasound attenuation quantitatively using PE is difficult due to various uncertainties arising in this peculiar case, including a complex source, possible invalidity of the underlying approximations discussed in Waxler and Assink (2019) and biases in wind field from climatology, gravity-wave perturbation or even reanalysis (e.g., Podglajen et al., 2014). Hence, PE simulations are only used here as a pedagogical tool to contextualize differences between receivers.

3. Results

3.1. First Infrasound Arrivals

Pressure spectrograms during the first overpass of the waves (Figure 2) show arriving first the low-frequency Lamb wave pulse (Matoza et al., 2022; Vergoz et al., 2022; Wright et al., 2022) extending up to $\sim 3 \text{ mHz}$. Above

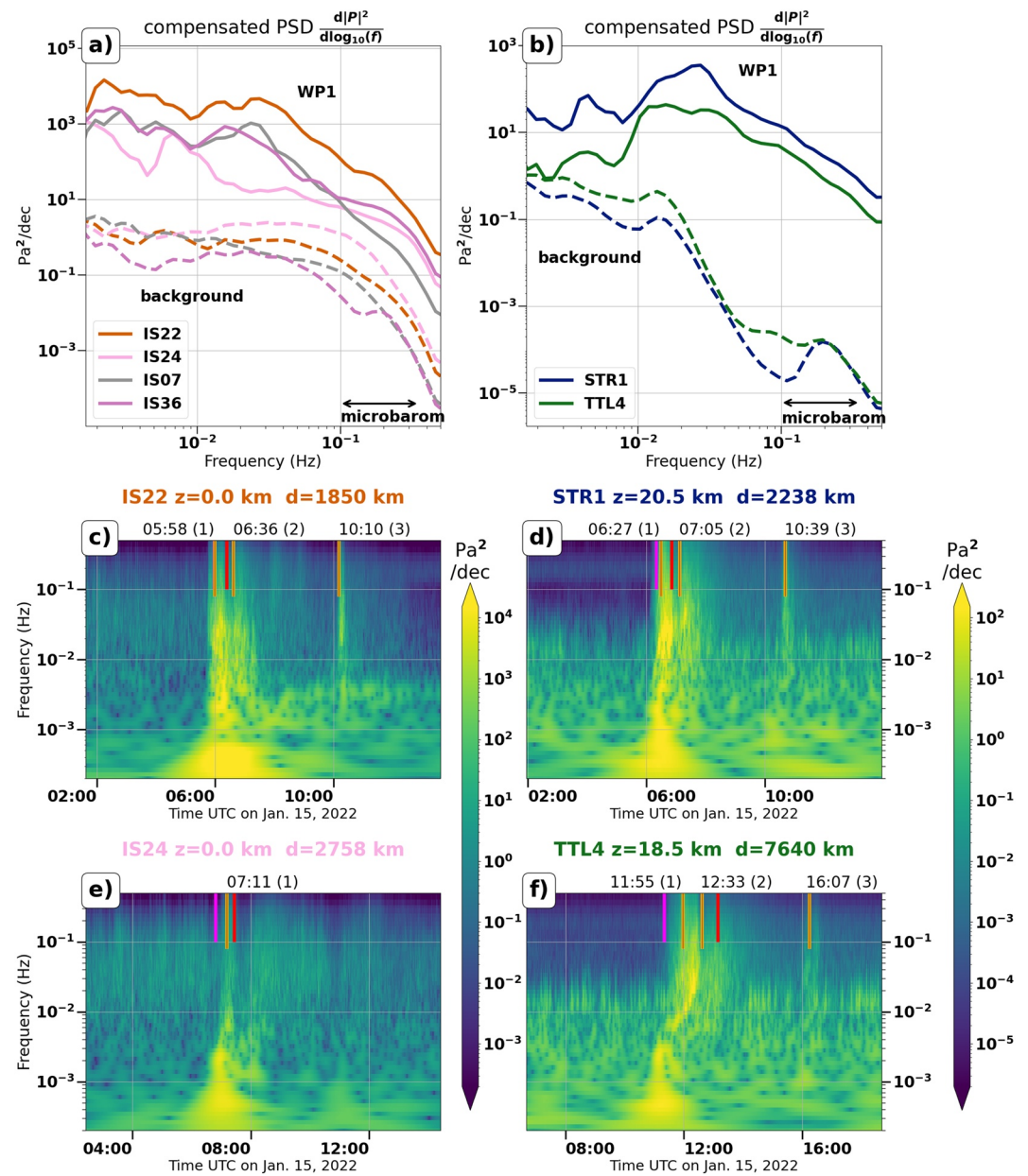


Figure 2. Compensated power spectral density (PSD multiplied by frequency) during the overpass of WP1 (solid line) and background of the 3 hr before the eruption (dashed line) for (a) the ground stations and (b) the balloons. (c–e), (f) Selected spectrograms of the pressure signals corresponding to the first wave arrivals. The orange vertical lines indicate arrival times of wavepackets (WPs) (timings reported above). Purple and red lines correspond to expected arrival times for the first event (see text) assuming travel speeds $c_g = 300$ m/s and $c_g = 240$ m/s, respectively.

~ 10 mHz, instead of a single pulse, several receivers (e.g., IS22, STR1, Figure 2) recorded a complex infrasound arrival sequence within which one may identify at least three distinct initial wavepackets (WPs) peaking around 20–30 mHz. WPs onsets, separated by periods of reduced acoustic power, are highlighted in Figure 2. The delay between WP1&3 is without ambiguity beyond the spread in arrival times which can be expected for acoustic wave generated by a unique trigger. As for WP1&2, the roughly constant time separation observed among receivers at different short-range distances and azimuths from Hunga (IS22, STR1), together with the absence of similar duplication of WP3, rules out differential propagation. Overall, this suggests that the WPs originate from successive source-level events. Dispersion, however, manifests itself at larger distances, creating longer, duplicated wavepackets at TTL4 (in particular WP3).

Taking advantage of the reproducible and highly structured arrival sequence, we deduce approximate average travel speed c_g for the different sensors, as explained in Text S2 in Supporting Information S1. c_g values (Table 1) vary consistently with prevailing stratospheric wind conditions (weakest to the East of the volcano, strongest to the West). Back-propagating WPs to the source suggests pulses of emission around 04:15, 04:53 and 08:27 (± 5 min). This chronology will be further discussed in Section 4.1.

10-min-averaged spectra at the arrival of WP1 (Figures 2a and 2b) show a significant enhancement in acoustic power over the whole acoustic range (above 10 mHz), corresponding to pressure fluctuations with standard deviation in the order of 5 Pa (STR1, TTL4) to more than 30 Pa (IS22). The spectra exhibit a peak at around 20–30 mHz, especially striking for balloon sensors. WP2 has somewhat higher frequency, peaking around 30–40 mHz in balloon records, and generally smaller amplitudes.

Besides distinct WPs, balloon observations exhibit a lasting tail of enhanced acoustic variability above 0.01 Hz with a return to pre-eruption levels after about a day. This feature is akin to the Coda observed in seismic waves (e.g., Aki, 1997) and likely results from multipathing and wave scattering by small-scale inhomogeneities, for example, pre-existing gravity waves (Chunchuzov et al., 2011).

3.2. Anisotropy of Infrasound Propagation

A large spread in infrasound-signal amplitude is found among receivers, as summarized in Table 1, which reports observed transmission losses with respect to IS22 for the 3 WPs. This anisotropy results from the variability of along-path stratospheric winds near Hunga (Figure 1a), which imply large variations in the associated c_{eff} profiles (Figure 1b) and infrasound ducting efficiency.

To illustrate this, selected T_L sections, estimated with ePape for a ground source of frequency 0.05 Hz, are displayed in Figure 1. Toward IS22, strong tailwinds support a stratospheric duct from ~ 50 km down to the ground (Figure 1c), explaining low attenuations for receivers West of the volcano (IS07, IS36, IS40). In other directions (STR1, IS24), head- and crosswinds hamper propagation at the surface. Nevertheless, a shallower duct exists, tied to the temperature minimum around the tropopause and confined to the UTLS. We will refer to it as the UTLS duct. This duct generates larger scaled amplitudes $|\tilde{P}|$ at stratospheric balloon flight altitude (Figures 1d and 1e).

Despite the qualitative agreement with Table 1 for each WP taken separately, this reasoning does not explain the observed increase in IS22-relative attenuations from WP1 to WP3. As reported by Matoza et al. (2022), the scatter in T_L is also smaller than in PE simulations forced at ground level. Besides dispersion, model biases and violated assumptions (e.g., linearity), these discrepancies likely partly arise due to the complexity of the time-varying source (Matoza et al., 2022). While a detailed assessment is beyond the scope of our study, we note that a possible (but not sole) contributing factor may be the event-dependent vertical distribution of the forcing. Indeed, Figure 1 suggests that significant generation at upper levels (here 20 km) tends to reduce anisotropy compared to lower-level sources.

3.3. Multiple Revolutions of Acoustic Waves

Longer recordings over the days following the eruption reveal multiple revolutions of infrasound waves (Vergoz et al., 2022), as shown for the balloons and nearby stations IS22 and IS57 in Figure 3. In the following, we adopt the convention for successive passages of Matoza et al. (2022); Vergoz et al. (2022): A1 for the direct (short-orthodrome) arrival, A2 for the first antipodal arrival, A3 for A1 + one revolution etc. Ground measurements are polluted by sporadic bursts of noise related to atmospheric turbulences, which prevent detections under high surface-wind conditions beyond A1 (Vergoz et al., 2022). A clearer picture emerges from balloon observations (Figures 3b and 3d), which almost exclusively exhibit geophysical signals above 30 mHz, and record clear arrivals up to A10 at STR1.

Figures 3e–3n highlights distinct acoustic dispersion patterns in panels a–d, which are described in the following. Although dispersion mixes A2 and A3 at STR1 (Figure 3e), one can clearly distinguish an A2 wavetrain with virtually no dispersion (“compact mode”) retaining the imprint of the source (i.e., distinct WP1 and WP2) over several revolutions. This mode has typical round-the-world-transit speed of 288 m/s (± 1 m/s). It is visible only at STR1, at least for passages A2 and A4 (Figure 3f). On Figure 3e, a second wavetrain (“dispersive modes”)

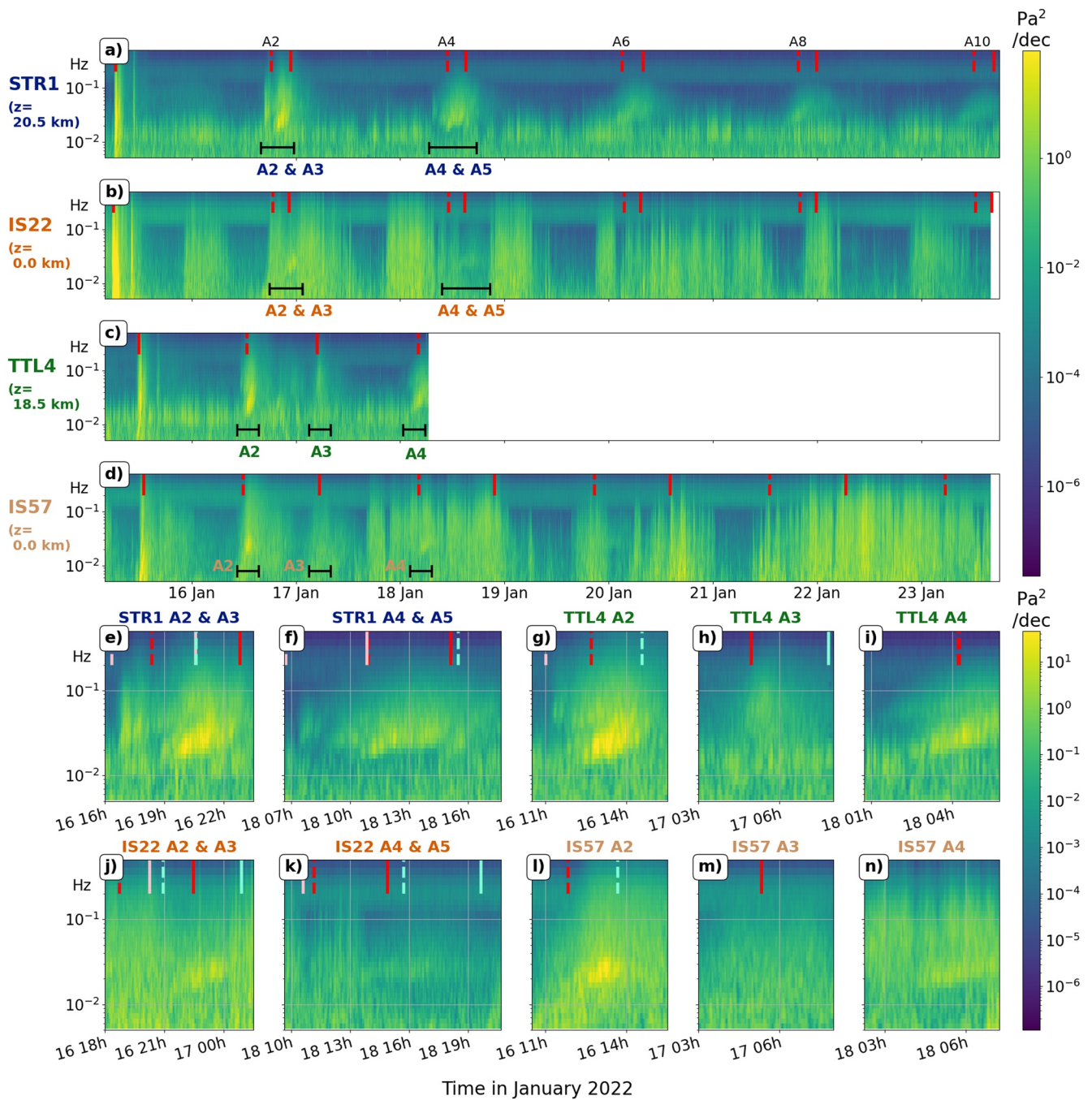


Figure 3. Spectrograms of the pressure signals at balloons (a) STR1 and (c) TTL4 and ground stations (b) IS22 and (d) IS57. Expected arrival times are shown for the 275 (red) m/s travel speed (solid lines for “direct,” dashed for antipodal). TTL4 time series stop on January 18 due to its burst. (e–n) Zoom on the (e, g, j, and l) first antipodal arrival and (e, h, j, and m) second direct and (f, i, k, and n) antipodal arrivals at (e–i) the balloons and (j–n) ground stations. Direct and antipodal arrivals superpose partly at STR1 and IS22. Further expected arrival times for 290 (pink) and 260 (light green) m/s propagation speeds are displayed.

follows. It is typically slower (~ 275 m/s), mixes with A3, and features two dispersion lines around 20 and 70 mHz. A double dispersion line was also observed for A1 in Kenya ($d = 15,750$ km) (Vergoz et al., 2022). The 70 mHz dispersive mode is also evident in passages A2 and A4 at TTL4 (Figures 3g and 3i) but absent at IS57 (Figures 3l and 3n). The lower (20 mHz) dispersion curve is longer-lived and appears at least at A2–4 at TTL4 and A2–10 at STR1, as well as at IS22 and IS57. From the spectrograms (Figure 3a), we estimate $\frac{\partial c_g}{\partial f} \approx -500\text{--}600$ m for this mode. This decrease in travel speed with frequency results in a flattening of the wave trains in frequency-time

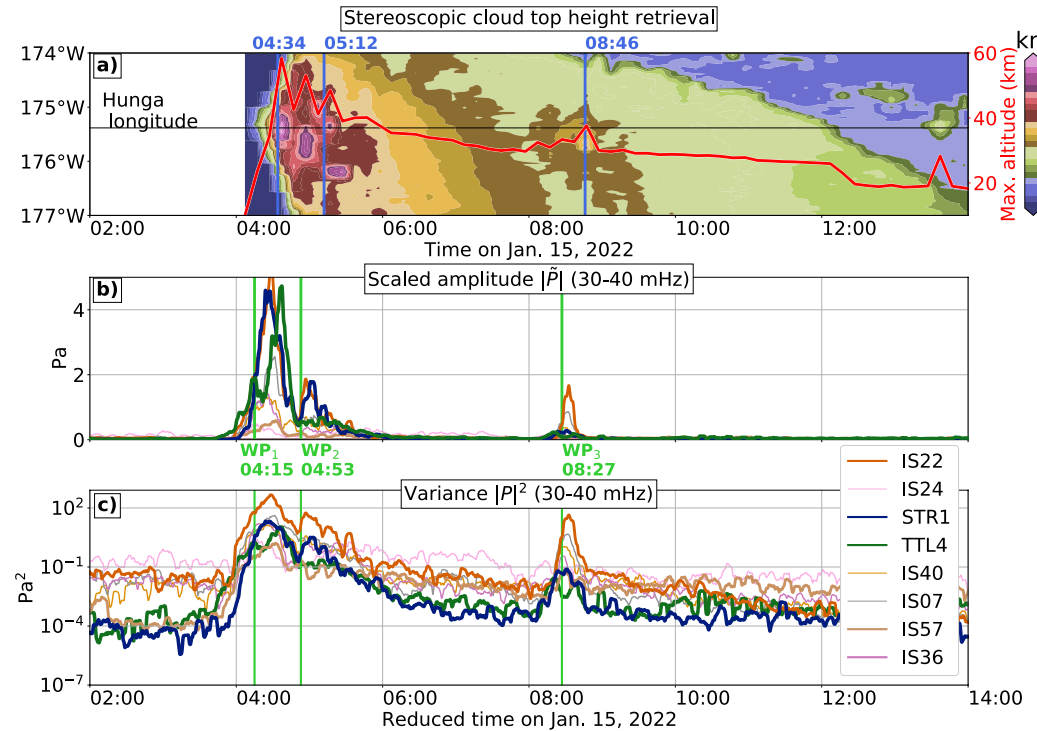


Figure 4. (a) Hovmöller diagram of plume top altitude and (red line) time series of maximum plume height in the area (20.75°S–20.35°S, 175.7°W–175.3°W). (b) 3-min scaled pressure amplitude $|\hat{P}|$ time series (30–40 mHz filtered) for selected receivers. The reference in Equation 2 is here chosen at STR1 ($\rho_r = 0.08 \text{ kg/m}^3$, $d_r = 2, 210 \text{ km}$). (c) 3-min $|P|^2$ variance (30–40 mHz). Green vertical lines are time onsets of wavepackets (WPs), and blue ones are the same shifted by 19 min. The time axis represents range-corrected reduced time $t_r = t - \frac{d}{c_g}$ from Table 1.

space over successive circumnavigations (Figures 3a–3d). Finally, for completeness, a non-dispersive 30-mHz wavepacket was recorded for A3 at TTL4, although not at IS57 (Figures 3h–3m).

The nature of this family of modes remains unclear. Their typical celerity resembles stratosphere-ducted infrasound with wind bringing substantial contribution in one or the other direction. Contrasted efficiency of wind ducting in different propagation directions likely plays a role in the favored “antipodal” propagation of the dispersive modes found at TTL4. It is noteworthy that, whereas ground stations IS22 measures larger amplitudes for A1, the situation reverses for later overpasses. For instance, the signal amplitude near the lower dispersion curve for passages A2 and A4 seems systematically larger at balloon altitude. Some arrivals clearly detected in the balloon signals are not discernible in ground recordings (e.g., at TTL4, the upper dispersion line for A2 and A4 or the A3 arrival). Altogether, this suggests that long-lived modes are ducted at upper levels, although their vertical structure and the role of wind in supporting them warrants further investigations.

4. Discussion

4.1. Infrasound Emission and Chronology of the Eruption

In Section 3.1, we argued that STR1 and IS22 captured the same infrasound emission sequence. The inferred scenario is substantiated in Figure 4, which depicts shifted time series of 3-min 30–40 mHz-filtered (Figure 4c) signal variance (proportional to acoustic power) and (Figure 4b) scaled amplitude for selected receivers. High correlations with IS22 are seen for other shorter-range sensors at various distances West of Hunga (IS07, IS40, IS36). They benefit from limited dispersion effects, likely thanks to the source proximity and overall similar (and favorable) propagation conditions (Vergoz et al., 2022). In contrast, signals are less distinct East of Hunga (IS24). Interestingly, balloon STR1 exhibits the highest correlation with IS22 around WP1&2 and has similar scaled amplitude $|\hat{P}|$.

Distinct WPs likely mirror different phases of acoustic-wave emission at the source. Vergoz et al. (2022) found that infrasound and seismic wave activity coincide for the early part of the eruption but decouple at later stages (i.e., WP 3). In very different eruptive contexts, previous studies (e.g., Fee et al., 2010) have found a correlation between radiated acoustic power and plume height. To explore this link with volcanic aerial activity, Figure 4a) presents the evolution of maximum plume altitude from stereoscopic CTH retrievals during the eruption. Notwithstanding a ~20-min delay between the onsets of infrasound WPs and observations of plumes reaching their ceiling, a rough match may be found between (a) WP1 and the first plume reaching the mesosphere (04:37), and (b) WP3 and a later plume observed reaching 38 km at 08:47. The higher initial plume also seems associated with larger infrasound power (Figure 4) and smaller anisotropy (Section 3.2) than the lower-height 08:47 injection. Contrary to WP1 and 3, tentative attribution of WP2 is not obvious. The second extended mesospheric intrusion occurs slightly West of Hunga and closely follows the first in time. CTH data also indicate a 48-km overshoot at Hunga's location at 05:17 which may better correspond. Event identification is challenging and not always meaningful given the complexity of the plume evolution and sources at play. Nevertheless, the comparison tends to suggest a significant role of processes related to plume dynamics (Fee & Matoza, 2013; Matoza et al., 2009; Watson et al., 2022; Woulff & McGetchin, 1976) in Hunga infrasound generation. It highlights the value of STR1's records which, gathered inside a waveguide, appear well-placed for source characterization.

The presented scenario of intermittent aerial activity is generally consistent with other atmospheric records of the event (e.g., Astafyeva et al., 2022; Vergoz et al., 2022; Wright et al., 2022). For example, ground pressure measurements at Nukua'lofa (Tonga, $d = 64$ km) show four major pressure minima (Wright et al., 2022), three of which closely match our WPs (04:36, 05:10 and 08:46). However, no enhanced infrasound corresponds to the third minimum (~05:51).

4.2. Advantages and Potential Limitations of Balloon Measurements

Our study evidences an infrasound SNR improved by a factor of at least 10 at lower stratospheric altitudes compared to the ground (Figures 2a, 2b, and 4). Reasons include (a) the location of the receiver inside the UTLS waveguide and (b) reduced noise in the absence of wind relative to the sensor (Bowman & Krishnamoorthy, 2021; Bowman & Lees, 2015; Krishnamoorthy et al., 2020).

For a ground source, infrasound signals are larger at the surface in conditions supporting deep propagation (West of Hunga). However, upper-air reception appears favored in otherwise unfavorable propagation conditions (IS21, Figure 1e). In general, the strong anisotropy observed for ground receivers is mitigated at UTLS levels, an advantage reinforced for sources around the UTLS duct (Figure 1e). This property is exacerbated in the case of Hunga for long-range paths from multiple circumnavigations, for which larger signals are encountered in the stratosphere.

Ground-level winds exceeding a few m/s (Vergoz et al., 2022) typically result in a background noise level (IPI^2) about three orders of magnitude larger at IMS stations than recorded onboard the balloons, as shown in Figure 4. Turbulence-induced noise is a well-known challenge of ground-based infrasound monitoring (e.g., Marty, 2019). Under low surface winds, reduced noise at the ground may be associated with better SNR there, as detailed in Text S4 of Supporting Information S1.

Despite its assets, the balloon platform might suffer from specific biases. One is related to the balloons oscillations (Massman, 1978), which are only partially corrected by the current implementation of Equation 1 (see Supporting Information S1 for further discussion). Others may be unanticipated. For instance, Garcia et al. (2022) recently identified a mismatch between balloon observations and pressure fluctuations expected from large-incidence infrasound generated by seismic waves. Those authors ruled out resonant excitation of pendulum oscillations and proposed that the observed discrepancies are induced by movements of the balloon/gondola system. For Hunga infrasound, we argue that the repeated recordings of continuous dispersion curves in the infrasound range between 10 and 100 mHz (Figure 3) advocate against large artifacts related to resonance at specific frequencies, demonstrating that pressure measurements onboard balloons are quantitatively reliable for shallow-angle-of-incidence infrasound waves.

5. Conclusions

The cataclysmic 15 January 2022 eruption of the Hunga volcano triggered a wide spectrum of atmospheric waves unprecedented in modern observational records. Located 2,200 and 7,800 km away from the volcano, two long-duration stratospheric balloons measured a clear signature of the surface-guided Lamb wave and of infrasound waves. Supported by plume top height data, the first arrival of infrasound wave packets at frequencies between 0.02 and 0.05 Hz indicate several bursts of acoustic wave emission highlighting a complex eruption scenario. Later infrasound arrivals associated with multiple revolutions (up to A10) could be detected until the end of the flights, 9 days after the eruption, corresponding to wavepackets circumnavigating the globe 5 times.

Together with balloon-borne infrasound earthquake (Brissaud et al., 2021; Garcia et al., 2022), surface (Bowman & Albert, 2018; Young et al., 2018) and underground (Bowman & Krishnamoorthy, 2021) explosion detections, this exceptionally long-range detection of acoustic waves from the Hunga eruption demonstrates the potential of long-duration stratospheric balloons for the monitoring of natural and anthropogenic hazards. Shortcomings of the 2021 Strateole-2 infrasound payload are (a) the limited time resolution of pressure measurements (1 Hz) and (b) the lack of azimuth and incidence angle measurements. The former will be improved in future campaigns by increasing the sampling rate of pressure measurements. For the latter, different teams recently tried to cover the gap with IMUs (Bowman et al., 2022; Garcia et al., 2020) or antennas of pressure sensors (Garcia et al., 2020; Krishnamoorthy et al., 2019). We recommend including such dedicated instrumentation in the future to provide additional constraint on wave properties. Finally, the response of SPBs to high-frequency atmospheric excitations is prone to significant uncertainties (Garcia et al., 2022; Podglajen et al., 2016). Further theoretical investigations are warranted to improve inferences on atmospheric wave properties from this invaluable platform (Bowman et al., 2022).

Data Availability Statement

Strateole-2 data is available at <https://data.ipsl.fr/catalog/strateole2/eng/catalog.search#/search?from=1&to=30>. IMS data is available upon request at <https://www.ctbto.org/specials/vdec> (last accessed on 2022-05-11). ECMWF data can be found at <https://cds.climate.copernicus.eu/cdsapp%23%21/dataset/reanalysis%2Dera5%2Dpressure%2Dlevels%3Ftab%3Dform> (last accessed on 2022-05-11). GOES-17 and Himawari-8 datasets are publicly accessible through Amazon Web Services (AWS). AWS Open Data description pages: <https://registry.opendata.aws/noaa-goes/> and <https://registry.opendata.aws/noaa-himawari/>.

Acknowledgments

The authors thank Daniel Bowman, David Fee and Alex Iezzi for insightful reviews, and Alain Hauchecorne and François Lott for discussions. The sponsorship of CNES, CNRS-INSU and NSF to Strateole-2 balloon activities is gratefully acknowledged.

References

- Aki, K. (1997). Seismic coda waves: A stochastic process in Earth's lithosphere. In S. A. Molchanov & W. A. Woyczynski (Eds.), *Stochastic models in geosystems* (pp. 1–24). Springer. https://doi.org/10.1007/978-1-4613-8500-4_1
- Astafeyeva, E., Maletkii, B., Mikesell, T. D., Munaibari, E., Ravanelli, M., Coisson, P., et al. (2022). The 15 January 2022 Hunga Tonga eruption history as inferred from ionospheric observations. *Geophysical Research Letters*, *49*(10), e2022GL098827. <https://doi.org/10.1029/2022GL098827>
- Bowman, D. C., & Albert, S. A. (2018). Acoustic event location and background noise characterization on a free flying infrasound sensor network in the stratosphere. *Geophysical Journal International*, *213*(3), 1524–1535. <https://doi.org/10.1093/gji/ggy069>
- Bowman, D. C., & Krishnamoorthy, S. (2021). Infrasound from a buried chemical explosion recorded on a balloon in the lower stratosphere. *Geophysical Research Letters*, *48*(21), e2021GL094861. <https://doi.org/10.1029/2021GL094861>
- Bowman, D. C., & Lees, J. M. (2015). Infrasound in the middle stratosphere measured with a free-flying acoustic array. *Geophysical Research Letters*, *42*(22), 10010–10017. <https://doi.org/10.1002/2015GL066570>
- Bowman, D. C., & Lees, J. M. (2018). Upper atmosphere heating from ocean-generated acoustic wave energy. *Geophysical Research Letters*, *45*(10), 5144–5150. <https://doi.org/10.1029/2018GL077737>
- Bowman, D. C., Rouse, J. W., Krishnamoorthy, S., & Silber, E. A. (2022). Infrasound direction of arrival determination using a balloon-borne aeroseismometer. *JASA Express Letters*, *2*(5), 054001. <https://doi.org/10.1121/10.0010378>
- Brissaud, Q., Krishnamoorthy, S., Jackson, J. M., Bowman, D. C., Komjathy, A., Cutts, J. A., et al. (2021). The first detection of an earthquake from a balloon using its acoustic signature. *Geophysical Research Letters*, *48*(12), e2021GL093013. <https://doi.org/10.1029/2021GL093013>
- Carr, J. L., Horváth, Á., Wu, D. L., & Friberg, M. D. (2022). Stereo plume height and motion retrievals for the record-setting Hunga Tonga-Hunga Ha'apai Eruption of 15 January 2022. *Geophysical Research Letters*, *49*(9), e2022GL098131. <https://doi.org/10.1029/2022GL098131>
- Chunchuzov, I. P., Kulichkov, S. N., Popov, O. E., Waxler, R., & Assink, J. (2011). Infrasound scattering from atmospheric anisotropic inhomogeneities. *Izvestiya - Atmospheric and Oceanic Physics*, *47*(5), 540–557. <https://doi.org/10.1134/S0001433811050045>
- Drob, D. P., Emmert, J. T., Meriwether, J. W., Makela, J. J., Doornbos, E., Conde, M., et al. (2015). An update to the Horizontal Wind Model (HWM): The quiet time thermosphere. *Earth and Space Science*, *2*(7), 301–319. <https://doi.org/10.1002/2014EA000089>
- Ern, M., Hoffmann, L., Rhode, S., & Preusse, P. (2022). The mesoscale gravity wave response to the 2022 Tonga volcanic eruption: Airs and MLS satellite observations and source backtracing. *Geophysical Research Letters*, *49*(10), e2022GL098626. <https://doi.org/10.1029/2022GL098626>

- Fee, D., Garcés, M., & Steffke, A. (2010). Infrasound from Tungurahua volcano 2006–2008: Strombolian to Plinian eruptive activity. *Journal of Volcanology and Geothermal Research*, 193(1), 67–81. <https://doi.org/10.1016/j.jvolgeores.2010.03.006>
- Fee, D., & Matoza, R. S. (2013). An overview of volcano infrasound: From Hawaiian to Plinian, local to global. *Journal of Volcanology and Geothermal Research*, 249, 123–139. <https://doi.org/10.1016/j.jvolgeores.2012.09.002>
- Garcia, R. F., Klotz, A., Hertzog, A., Martin, R., G erier, S., Kassarian, E., et al. (2022). Infrasound from large earthquakes recorded on a network of balloons in the stratosphere. *Geophysical Research Letters*, 49(15), e2022GL098844. <https://doi.org/10.1029/2022GL098844>
- Garcia, R. F., Martire, L., Chaigneau, Y., Cadu, A., Mimoun, D., Portus, M. B., et al. (2020). An active source seismo-acoustic experiment using tethered balloons to validate instrument concepts and modelling tools for atmospheric seismology. *Geophysical Journal International*, 225(1), 186–199. <https://doi.org/10.1093/gji/ggaa589>
- Gardner, C. S., Hostetler, C. A., & Franke, S. J. (1993). Gravity wave models for the horizontal wave number spectra of atmospheric velocity and density fluctuations. *Journal of Geophysical Research*, 98(D1), 1035–1049. <https://doi.org/10.1029/92JD02051>
- Haase, J., Alexander, M. J., Hertzog, A., Kalnajs, L., Deshler, T., Davis, S., et al. (2018). Around the world in 84 days. *Eos*, 99. <https://doi.org/10.1029/2018eo091907>
- Hersbach, H., Bell, B., Berrisford, P., Hirahara, S., Hor anyi, A., Mu oz-Sabater, J., et al. (2020). The ERA5 global reanalysis. *Quarterly Journal of the Royal Meteorological Society*, 146(730), 1999–2049. <https://doi.org/10.1002/qj.3803>
- Hertzog, A., Cocquerez, P., Guilbon, R., Valdivia, J.-N., Venel, S., Basdevant, C., et al. (2007). Strat ole/vorcore—Long-duration, superpressure balloons to study the Antarctic lower stratosphere during the 2005 winter. *Journal of Atmospheric and Oceanic Technology*, 24(12), 2048–2061. <https://doi.org/10.1175/2007JTECHA948.1>
- Holasek, R. E., Self, S., & Woods, A. W. (1996). Satellite observations and interpretation of the 1991 mount Pinatubo eruption plumes. *Journal of Geophysical Research*, 101(B12), 27635–27655. <https://doi.org/10.1029/96jb01179>
- Hupe, P., Ceranna, L., Le Pichon, A., Matoza, R. S., & Mialle, P. (2022). International monitoring system infrasound data products for atmospheric studies and civilian applications. *Earth System Science Data Discussions*, 14(9), 1–40. <https://doi.org/10.5194/essd-14-4201-2022>
- Krishnamoorthy, S., Bowman, D. C., Komjathy, A., Pauken, M. T., & Cutts, J. A. (2020). Origin and mitigation of wind noise on balloon-borne infrasound microbarometers. *Journal of the Acoustical Society of America*, 148(4), 2361–2370. <https://doi.org/10.1121/10.0002356>
- Krishnamoorthy, S., Lai, V. H., Komjathy, A., Pauken, M. T., Cutts, J. A., Garcia, R. F., et al. (2019). Aerial seismology using balloon-based barometers. *IEEE Transactions on Geoscience and Remote Sensing*, 57(12), 10191–10201. <https://doi.org/10.1109/TGRS.2019.2931831>
- Marty, J. (2019). The IMS infrasound network: Current status and technological developments. In A. Le Pichon, E. Blanc, & A. Hauchecorne (Eds.), *Infrasound monitoring for atmospheric studies: Challenges in middle atmosphere dynamics and societal benefits* (pp. 3–62). Springer International Publishing. https://doi.org/10.1007/978-3-319-75140-5_1
- Massman, W. J. (1978). On the nature of vertical oscillations of constant volume balloons. *Journal of Applied Meteorology*, 17(9), 1351–1356. [https://doi.org/10.1175/1520-0450\(1978\)017<1351:otnovo>2.0.co;2](https://doi.org/10.1175/1520-0450(1978)017<1351:otnovo>2.0.co;2)
- Matoza, R. S., Fee, D., Assink, J. D., Iezzi, A. M., Green, D. N., Kim, K., et al. (2022). Atmospheric waves and global seismoacoustic observations of the January 2022 Hunga eruption, Tonga. *Science*, 377(6601), 95–100. <https://doi.org/10.1126/science.abo7063>
- Matoza, R. S., Fee, D., Garc es, M. A., Seiner, J. M., Ram on, P. A., & Hedlin, M. a. H. (2009). Infrasonic jet noise from volcanic eruptions. *Geophysical Research Letters*, 36(8), L08303. <https://doi.org/10.1029/2008GL036486>
- Mill n, L., Santee, M. L., Lambert, A., Livesey, N. J., Werner, F., Schwartz, M. J., et al. (2022). The Hunga Tonga-Hunga Ha'apai hydration of the stratosphere. *Geophysical Research Letters*, 49(13), e2022GL099381. <https://doi.org/10.1029/2022GL099381>
- Picone, J. M., Hedin, A. E., Drob, D. P., & Aikin, A. C. (2002). NRLMSISE-00 empirical model of the atmosphere: Statistical comparisons and scientific issues. *Journal of Geophysical Research*, 107(A12), SIA15-1–SIA15-16. <https://doi.org/10.1029/2002JA009430>
- Pierce, A. D., & Posey, J. W. (1971). Theory of the excitation and propagation of lamb's atmospheric edge mode from nuclear explosions. *Geophysical Journal International*, 26(1–4), 341–368. <https://doi.org/10.1111/j.1365-246X.1971.tb03406.x>
- Podglajen, A., Hertzog, A., Plougonven, R., & Legras, B. (2016). Lagrangian temperature and vertical velocity fluctuations due to gravity waves in the lower stratosphere. *Geophysical Research Letters*, 43(7), 3543–3553. <https://doi.org/10.1002/2016GL068148>
- Podglajen, A., Hertzog, A., Plougonven, R., &  agar, N. (2014). Assessment of the accuracy of (re)analyses in the equatorial lower stratosphere. *Journal of Geophysical Research: Atmospheres*, 119, 11166–11188. <https://doi.org/10.1002/2014JD021849>
- Poli, P., & Shapiro, N. M. (2022). Rapid characterization of large volcanic eruptions: Measuring the impulse of the Hunga Tonga Ha'apai explosion from teleseismic waves. *Geophysical Research Letters*, 49(8), e2022GL098123. <https://doi.org/10.1029/2022GL098123>
- Proud, S. R., Prata, A., & Schmauss, S. (2022). The January 2022 eruption of Hunga Tonga-Hunga Haapai volcano reached the mesosphere. *Earth and Space Science Open Archive*, 11. <https://doi.org/10.1002/essoar.10511092.1>
- Sellitto, P., Podglajen, A., Belhadji, R., Boichu, M., Carboni, E., Cuesta, J., et al. (2022). The unexpected radiative impact of the Hunga Tonga eruption of January 15th (p. 202). <https://doi.org/10.21203/rs.3.rs-1562573/v1>
- Vergoz, J., Hupe, P., Listowski, C., Le Pichon, A., Garc es, M. A., Marchetti, E., et al. (2022). IMS observations of infrasound and acoustic-gravity waves produced by the January 2022 volcanic eruption of Hunga, Tonga: A global analysis. *Earth and Planetary Science Letters*, 591, 117639. <https://doi.org/10.1016/j.epsl.2022.117639>
- Vincent, R. A., & Hertzog, A. (2014). The response of superpressure balloons to gravity wave motions. *Atmospheric Measurement Techniques*, 7(4), 1043–1055. <https://doi.org/10.5194/amt-7-1043-2014>
- Watson, L. M., Iezzi, A. M., Toney, L., Maher, S. P., Fee, D., McKee, K., et al. (2022). Volcano infrasound: Progress and future directions. *Bulletin of Volcanology*, 84(5), 44. <https://doi.org/10.1007/s00445-022-01544-w>
- Waxler, R., & Assink, J. (2019). Propagation modeling through realistic atmosphere and benchmarking. In A. Le Pichon, E. Blanc, & A. Hauchecorne (Eds.), *Infrasound monitoring for atmospheric studies: Challenges in middle atmosphere dynamics and societal benefits* (pp. 509–549). Springer International Publishing. https://doi.org/10.1007/978-3-319-75140-5_15
- Waxler, R., Hetzer, C., Assink, J., & Velea, D. (2021). Chetzer-ncpa/ncpprop-release: NCPAprop v2.1.0. *Zenodo*. <https://doi.org/10.5281/zenodo.5562713>
- Woulff, G., & McGetchin, T. R. (1976). Acoustic noise from volcanoes: Theory and experiment. *Geophysical Journal International*, 45(3), 601–616. <https://doi.org/10.1111/j.1365-246X.1976.tb06913.x>
- Wright, C. J., Hindley, N. P., Alexander, M. J., Barlow, M., Hoffmann, L., Mitchell, C. N., et al. (2022). Surface-to-space atmospheric waves from Hunga Tonga-Hunga Ha'apai eruption. *Nature*, 609(7928), 741–746. <https://doi.org/10.1038/s41586-022-05012-5>
- Young, E. F., Bowman, D. C., Lees, J. M., Klein, V., Arrowsmith, S. J., & Ballard, C. (2018). Explosion-generated infrasound recorded on ground and airborne microbarometers at regional distances. *Seismological Research Letters*, 89(4), 1497–1506. <https://doi.org/10.1785/0220180038>
- Yuen, D. A., Scruggs, M. A., Spera, F. J., Zheng, Y., Hu, H., McNutt, S. R., et al. (2022). Under the surface: Pressure-induced planetary-scale waves, volcanic lightning, and gaseous clouds caused by the submarine eruption of Hunga Tonga-Hunga Ha'apai volcano provide an excellent research opportunity. *Earthquake Research Advances*, 2(3), 100134. <https://doi.org/10.1016/j.eqrea.2022.100134>